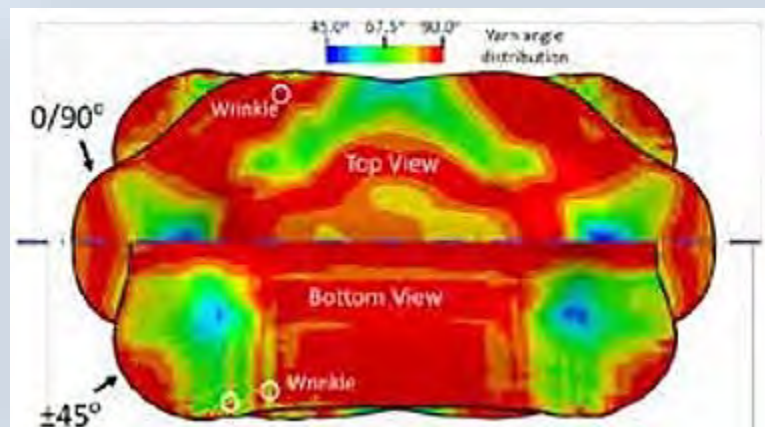


FEA Information Engineering Journal



Article: A non-orthogonal material model of woven composites in the preforming process.

Editors: Yanhua Zhao - Marsha Victory

yanhua@feainformation.com

Aim and Scope

FEA Information Engineering Journal (FEAIEJ™) is a quarterly published online journal to cover the latest Finite Element Analysis Technologies. The journal aims to cover previous noteworthy published papers and original development updates. All published papers are peer reviewed in the respective FEA engineering fields.

Consideration is given to all aspects of technically excellent written information without limitation on length. All submissions must follow guidelines for publishing a paper, or periodical. If a paper has been previously published, FEAIEJ requires written permission to reprint, with the proper acknowledgement give to the publisher of the published work.

Reproduction in whole, or part, without the express written permission of FEA Information Engineering Journal, or the owner of of the copyright work, is strictly prohibited. FEAIJ welcomes unsolicited topics, ideas, and articles.

Monthly publication is limited to no more then five papers or informational articles of interest, either reprint, or original.

For information on publishing a paper original or reprint contact yanhua@feainformation.com
Subject line: Journal Publication

Cover:

Fig. Figure 8. Double dome preformed part of double-layer woven prepregs simulation result.

*Article: Double dome preformed part of double-layer woven prepregs simulation result.
A non-orthogonal material model of woven composites in the preforming process..*

TABLE OF CONTENTS

Publications are © to the authors and are informational publishings

All contents are copyright © to the publishing company, author or respective company. All rights reserved.

01. Modeling and Numerical Simulation of Afterburning of Thermobaric Explosives

In a Closed Chamber

Kyoung su Im, Grant Cook, Jr., and Zeng-Chan Zhang
Livermore Software Technology Corp.

02. A non-orthogonal material model of woven composites in the preforming process

a Weizhao Zhang#, aHuaqing Ren#, aBiao Liang, bDanielle Zeng, bXuming Su,

b Jeffrey Dahl,

c Mansour Mirdamadi,

d Qiangsheng Zhao, aJian Cao (1)

a Department of Mechanical Engineering, Northwestern University, Evanston, IL, USA

b Ford Motor Company, Dearborn, MI, USA

c Dow Chemical Company, Midland, MI, USA

d Livermore Software Technology

03. Conversion between FLD and Stress Triaxial Limit Curve

Xinhai Zhu, Li Zhang, and Yuzhong Xiao

LSTC

04..Best Fit GUI for Metal Forming in LS-PrePost® 4.5

Q. Yan, Xinhai Zhu, Philip Ho, Li Zhang, Yuzhong Xiao

LSTC

Modeling and Numerical Simulation of Afterburning of Thermobaric Explosives In a Closed Chamber

Kyoung su Im, Grant Cook, Jr., and Zeng-Chan Zhang
Livermore Software Technology Corp.

INTRODUCTION

Heterogeneous combustion (i.e., solid and gas or liquid and gas) has a wide range of applications such as solid rocket propulsion, combustion instability control, underwater explosion, and high energy explosion [1-4]. Among several possible combinations, the thermobaric explosive (TBX) composed of trinitrotoluene (TNT) and energetic metal particles (typically aluminum) is a widely used explosive and is of great importance in the safety, mining, and defense industries.

TBX (a thermobaric explosive) is defined as “a partially detonating energetic material with excess fuel (gas, solid or liquid) dispersed and mixed into air with subsequent ignition and reaction achieved in time and in place for added gain of energy, blast and heat.” As such, TBX has greatly enhanced thermal and blast effects compared to conventional high explosives [5].

In TBX flow, thermobaric effects are obtained by long-duration overpressure and heating due to the afterburning of detonation products in air. Since the afterburning process is controlled by turbulent mixing and combustion in air after detonation or dispersion by a bursting charge, even the identical explosive composition may yield different thermal and blast performance with different targets. Therefore, the detailed understanding of the afterburning mechanism is required to optimally design warheads for various operational environments. To this end, TBX module has been implemented in LS-DYNA®

MODEL VALIDATION WITH EXPERIMENT

Experiments in present investigation were carried out using a closed bomb test (CBT) chamber for model validation of the TBX afterburning processes. Figure 1 shows the schematics of the experimental chamber and an initial charge of TBX. The CBT chamber has a dimension of 40 cm in radius (r) and 150cm in longitudinal length (x) so that the total volume of the chamber is 0.754 m^3 . Two pressure gauges (Kulite; HEL-375-250A, and HEL-375-500A) having different sensing capacities were installed: one at the front enter of the cylinder ($x=750\text{cm}$, $r=40\text{cm}$) and the other at the side center of the cylinder base surface ($x=150\text{cm}$, $r=0\text{cm}$), respectively. The measured pressure data from the sensors were logged using the data acquisition system, DEWE-500, for analysis of the blast performance.

The cylindrical (30 mm in diameter and 33mm in length) Tritonal TBX charge weighs 40g and consists of well mixed TNT (80%) and aluminum particles (20%, with an average diameter of $10\mu\text{m}$). The main charge, combined with the blast cap (5g booster explosives of TNT compounds) and the exploding bridge wire (EBW) shown in Fig. 1(b) was initially located at the CBT center ($x=75\text{cm}$, $r=0\text{cm}$) of the CBT chamber for each experiment. Several experiments were conducted to obtain reliable data sets, and three data sets were collected with less than 10% standard relative error (SRE) from the average at each time instant. The pressure histories after explosion are illustrated in Fig. 2 at the side (a) and front center (b) of the CBT chamber.

Figure 2 shows the TBX validations with the pressure data sets for the side and front center position between the simulation results and averaged experimental data. Figure 2(a) and (b) illustrate the pressure history at the side and front center, respectively, and Figure 2(c) and (d) show the corresponding impulse, which is defined as pressure integrated over time. It is clear that the simulation results are in excellent agreement with the experimental data over the time ranges. At earlier time, the peak pressures slightly overshoot the measured data. In general, when the metal particles contribute to the afterburning in TBX, the peak pressure becomes lower but the impulse tends to be higher as the chamber pressure lasts longer than that of normal high explosives.

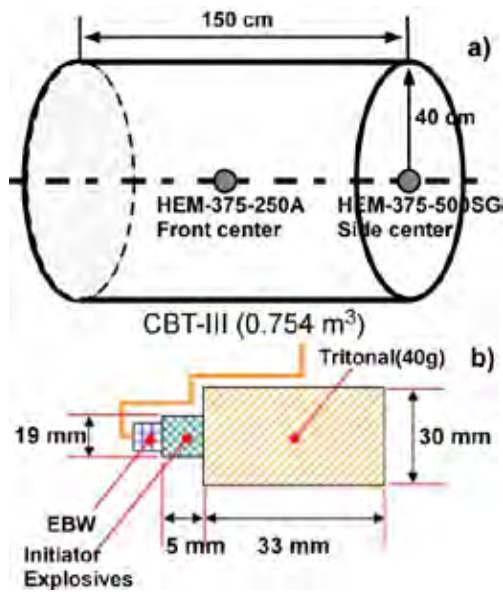


Figure 1

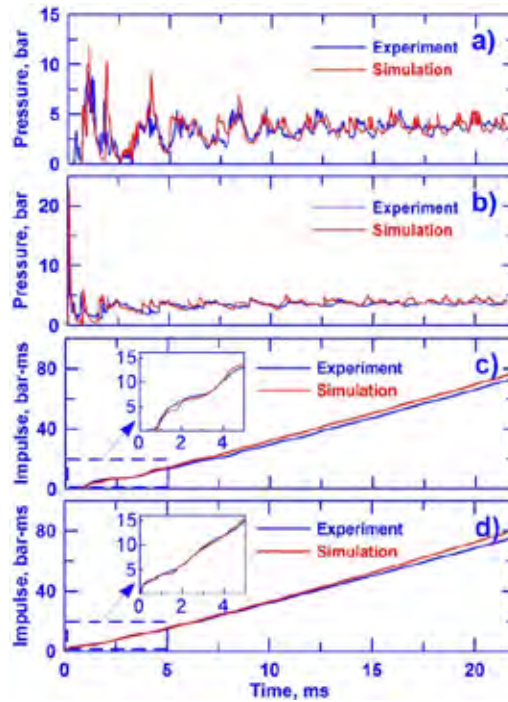


Figure 2

Figure 1 Schematics of the experimental closed bomb test chamber and the structure of the initial TBX: a) closed bomb test chamber with volume of 0.754 m^3 with two pressure sensing positions at front and side center, and b) the TBX charge structure consists of 40g of Tritonal and a blasting cap (initiator explosives, and an exploding bridge wire (EBW)).

Figure 2 Comparisons between measured data and simulation at the side and front center positions: a) and b) are the pressure histories, c) and d) are the impulses versus time.

BLAST PERFORMANCE

Prior to TBX simulation, the homogeneous calculation with only TNT explosive was conducted to better understand blast wave propagation and also to validate the developed code. Detailed geometrical setups and initial conditions can be found in Ref. [6]. Although the results are not provided, the over pressure histories in time [6] was validated as a preliminary calculation.

Figure 3 shows consecutive snapshots of the temperature distributions at different time instants showing the blast wave propagation procedures. After symmetric propagation and flame separation from a leading shock in Fig. 3(a) and (b), the shock wave hits the side walls and is reflected (Fig. 3(c)). Then, the flame starts to randomly mix as shown in Fig. 3(d)~3(f). At later times, the flames become more chaotically mixed as seen in Fig. 3(g)~3(i).

When the blast waves arrives at the side center, the pressure immediately peaks to its maximum value, and the reflected wave from the cylinder wall results in the subsequent peaks as the process repeats, conjugates, and dissipates until the pressure converges to an elevated value, but still with considerably noisy patterns after 5ms from the initial explosion.

PARTICLE DYNAMICS

Figure 4 illustrates the effects of particle dynamics on aluminum vaporization by varying the initial conditions such as mono-dispersed and Rosin-Rammler distributions, and different particle mean diameters, $10\mu\text{m}$, $20\mu\text{m}$, and $40\mu\text{m}$. The mono-dispersed distributions show a higher rate of vaporization in all cases. The deviations from the vaporization curves between the distributions are reduced with increasing diameter and eventually, there is little difference in the $40\mu\text{m}$ cases, in which the size distribution is no longer important in confined explosions. It is also obvious that the vaporization rates decrease almost linearly with increasing diameter. At $10 \mu\text{m}$, the particle

vaporization is about 80% of the initial aluminum particle mass. With doubled diameter, it is approximately reduced by factor of two. At 40 μm , it is cut down another half, much less than 20%. From these observations, the maximum contribution of metal combustion to the afterburning performance occurred at small particle diameter. But there might be a critical diameter to optimize the afterburning performance. Therefore, the proper selection of the particle diameter is of paramount importance in the manufacturing process of TBX.

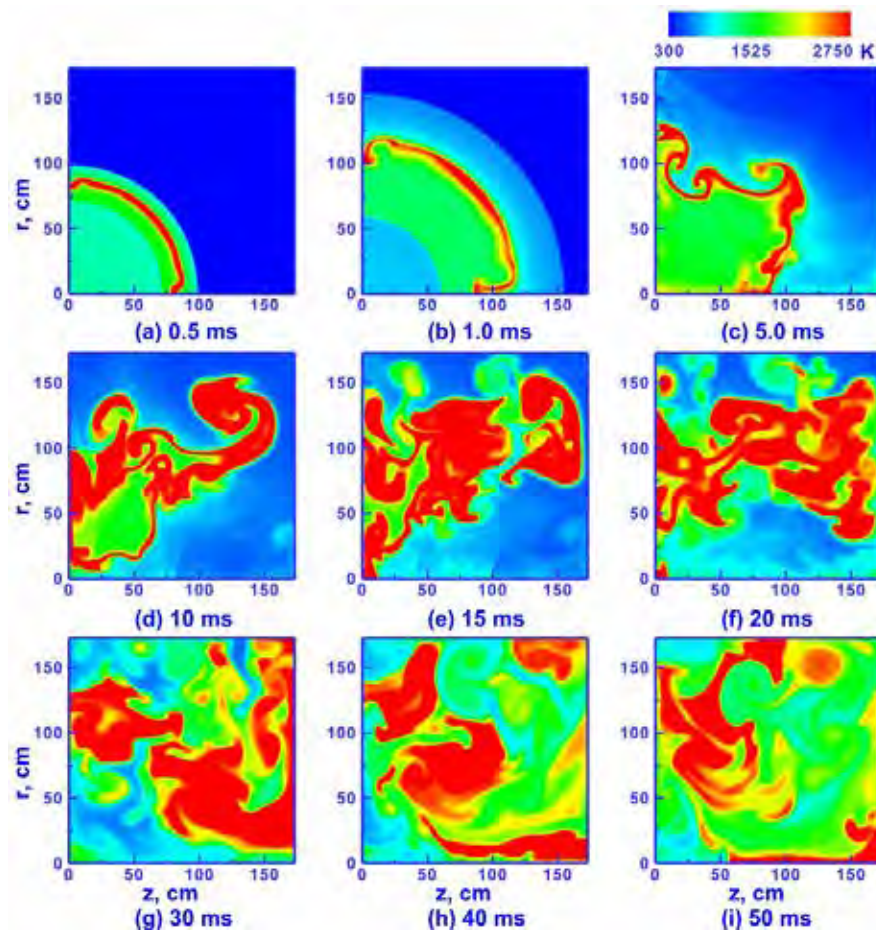


Figure 3 Consecutive snapshots of the temperature distributions at different time for the blast propagation.

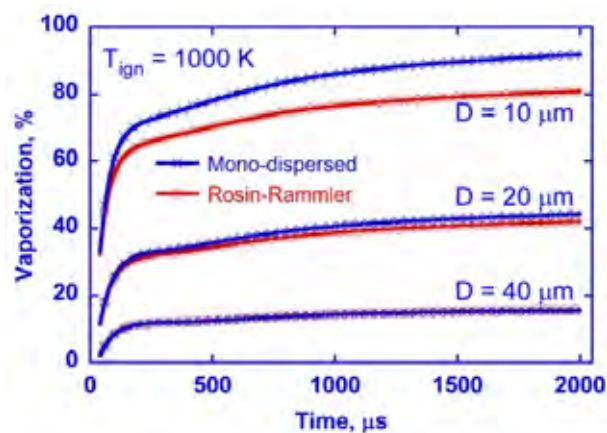


Figure 4 Aluminum vaporization rate according to particle distribution and different particle diameters.

INFORMATION: HOW TO USE

1. Prepare the chemistry input file (*.inp) and thermodynamics data files (thermo.dat) participated combustion species in the calculation.
2. Select the metal particle and set the initial condition using *STOCHASTIC_TBX_PARTICLES.
3. Set initial conditions and chemistry composition for the calculations.
4. Run the code to get the blast performance or TBX flow properties.

CONCLUSION

The present investigation has demonstrated an accurate and concrete model developed for the afterburning process of TBX combustion in conjunction with experimental validation in a confined chamber. The simulation for the afterburning of TBX, validated by the experimental data, clearly revealed the importance of the blast performance and particle dynamics, which should find broader applications in related industries by using the CE/SE and Chemistry solver in LS-DYNA.

REFERENCE

1. K. Kim, W. Wilson, J. Colon, T. Kreitingner, C. Needham, et. al., "Non-ideal explosive performance in a building structure," WIT Transaction on The Built Environment, 87, pp. 515-524, 2006.
2. J. Massoni, R. Saurel, A. Lefrancois, and G. Baudin, "Modeling spherical explosions with aluminized energetic materials," Shock Waves, Vol. 16, pp. 75-92, 2006.
3. E. W. Price, K. J. Kraeutle, J. L. Prentice, T. L. Boggs, J. E. Crump, and D. E. Zurn, "Behavior of Aluminum in Solid Propellant Combustion," NWC TP 6120, 1982.
4. C.-K. Kim, J. G. Moon, J.-S. Hwang, M.-C. Lai, and K.-S. Im , "Afterburning of TNT Explosive Products in Air with Aluminum Particles", AIAA Paper 2008-1029, 2008
5. A. L. Kuhl, R. E. Ferguson, and A. K. Oppenheim, "Gasdynamics Model of Turbulent Exothermic Fields in Explosions," Progress in Astronautics and Aeronautics Series, 173,AAA, Washington, D.C, pp. 251-261, 1997.
6. D. Schwer, and K. Kailasanath, "Blast Mitigation by Water Mist (1) Simulation of Confined Blast Waves," Technical Report NRL/MR/6410-02-8636, 2002.

A non-orthogonal material model of woven composites in the preforming process

^aWeizhao Zhang[#], ^aHuaqing Ren[#], ^aBiao Liang, ^bDanielle Zeng, ^bXuming Su, ^bJeffrey Dahl, ^cMansour Mirdamadi, ^dQiangsheng Zhao, ^aJian Cao (1)

^aDepartment of Mechanical Engineering, Northwestern University, Evanston, IL, USA

^bFord Motor Company, Dearborn, MI, USA

^cDow Chemical Company, Midland, MI, USA

^dLivermore Software Technology Corporation, Livermore, CA, USA

[#]Equal contribution

1. Introduction

Woven carbon fiber reinforced plastics (CFRPs) have received growing attentions from transportation industry because of their high performance to weight ratio [1, 2]. Due to its good geometric conformability, woven CFRP is most suitable for complex part geometries. A highly-automated process chain consisting of preforming and curing process developed recently to manufacture the CFRP parts at low cost and high speed. Materials used in the first preforming step is the stacked flat layers of prepregs, which are woven CFRPs impregnated with uncured thermoset resin in desired fiber orientations. These layers are heated above the resin melting temperature to fully soften the prepreg and formed into the part shape on a press. The formed part is then cured to harden the resin for the permanent shape [3].

There exists ample design freedom in woven CFRP products in terms of parameters or options in material design and preforming processes. The large consumption of the test material and the extensive experimental trial out period could lead to high developing cost and long product development cycle. Numerical methods that can simulate the preforming process should be developed in order to solve this problem [4].

A non-orthogonal model for the woven CFRP preforming process is developed in this work, which has been incorporated into the LS-DYNA[®] software as MAT_293 (MAT_COMPFRF) through the joint effort of this academic and industry team. Following in this paper is the detailed illustration of the fundamentals of this model and its experimental validation conducted at an industrial lab. Additionally, the measurement of interaction between prepreg layers is also characterized.

2. Analysis of the material deformation mechanism

Woven CFRPs are highly anisotropic in mechanical properties. The prepreg has large tensile modulus along the warp and weft yarn directions because of the stiff carbon fibers, but small intra-ply shear modulus, especially at the preforming temperature when the resin is molten as the shear resistance is mostly provided by the resin and the friction between the fiber yarns. During the preforming, the most dominant deformation mode is the intra-ply shear. To capture this mechanism, we propose to fully decouple the tension and shear deformation and the decoupling must hold well under large shear deformation.

Stress analysis for the woven CFRP with the modified non-orthogonal model is shown in Fig. 1. σ_{f1} and σ_{f2} are the stress components caused by yarn stretch, and they are along the warp and weft yarn directions, respectively. σ_{m1} and σ_{m2} are the stress components caused by the yarn rotation. These stress components will be transformed into the local corotational coordinate, summed up as σ_{xx} , σ_{xy} , and σ_{yy} , and will be the stress outputs reported from the material model to the FEM software.

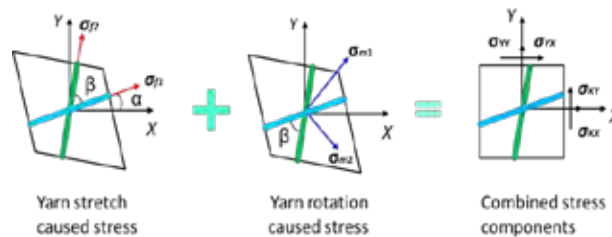


Fig. 1. Stress analysis of the woven CFRP with the modified non-orthogonal model.

The deformation gradient tensor \mathbf{F} is utilized in this model to trace the yarn directions and stretch ratios during the preforming via $\mathbf{g} = \mathbf{F} \cdot \mathbf{G}$, where \mathbf{g} and \mathbf{G} are the final and initial orientations of the local fibers respectively. It can be used to calculate α , which indicates the relative rotation between the local warp direction and the X -direction in the local corotational coordinate, and yarn angle β , which indicates the amount of shear deformation in the material.

The model was implemented into the FEM software LS-DYNA[®] as MAT_293 (MAT_COMPFRF). MAT_293 enables users to directly input experimental data to define the stress-strain curves, as well as the shear locking angle, which indicates whether the shear deformation reaches to the extent that the rotation resistance between warp and weft yarns is no longer small compared to the tensile modulus of the material. The flowchart of the model is shown in Fig. 2.

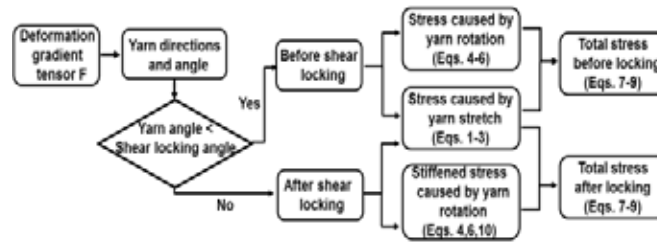


Fig. 2. Calculation flowchart of the LS-DYNA MAT_293.

In the material subroutine, the warp and weft directions for each element are calculated from the deformation gradient tensor. If the angle between the warp and weft yarns are smaller than the shear locking angle, then the small shear modulus condition will hold. If the angle between the warp and weft yarns reaches to the shear locking angle, the resistance for further shear deformation will greatly increase because the contacted fiber yarns stiffen the woven structure. In this situation, the shear resistance of the model will increase automatically to avoid further large shear deformation.

3. Material characterization

Material characterization is essential for the FEM model to predict the behavior of the woven CFRPs during the preforming process. It can be seen from Fig. 1 that the stresses caused by both yarn stretch and yarn rotation need to be calibrated for any specific woven material that is of interest. The calibration can be performed experimentally by the uniaxial tension and bias-extension tests [5]. The undulation strain and the stable tensile modulus along the yarn directions, as shown in Fig. 3(a), are obtained from the uniaxial tension test. In the FEM calculation, at every material point, once the stretch ratio along the yarns was obtained from the deformation gradient tensor, the resulting stress due to yarn stretch, i.e., “yarn stretch caused stress” σ_{f1} and σ_{f2} , can be obtained by referencing to the data in Fig. 3 (a). The shear behavior obtained via the bias-extension test, as shown in Fig. 3(b), is directly implemented as a polynomial function into the model to calculate the “yarn rotation caused stress” σ_{m1} and σ_{m2} given the angle change between the warp and weft yarns obtained from the deformation gradient tensor. The shear locking angle is also measured after the test and input to the model for the small/large shear moduli selection process shown in Fig. 2.

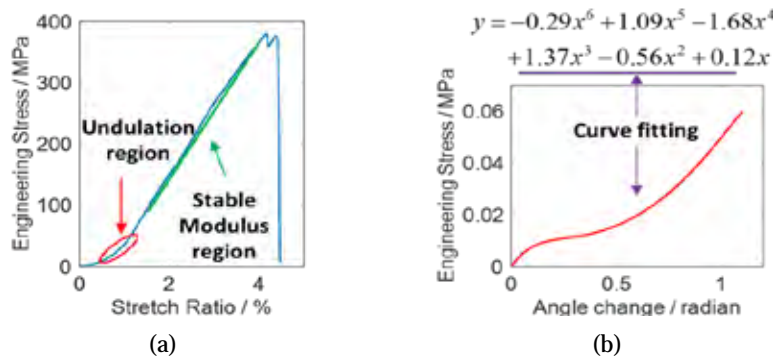


Fig. 3. (a) Uniaxial tension test result for undulation and tensile modulus characterization and (b) bias-extension test result for shear deformation characterization

However, these two tests only provide the in-plane intra-ply properties of the material. During the preforming simulation, the bending behavior of the single layer and the interaction between the composite layers will also affect the in-plane strain distribution and the wrinkling initiation. Hence, characterizations of bending stiffness and inter-ply interaction are also necessary.

Bending stiffness of the composite is characterized with the cantilever beam system, as shown in Fig. 4(a). During the test, the single-ply prepreg will deform under gravity and the deflection is measured by a digital image analysis system. A bending test simulation model is utilized for parameter calibration. Material properties such as tensile modulus and composite density are inputs to the FEM model. Then the compressive modulus is adjusted until the same displacement in the Y direction of the end tip as that in the experiment is achieved. The final bending profile will be compared as shown in Fig. 4(b) to confirm the approach.

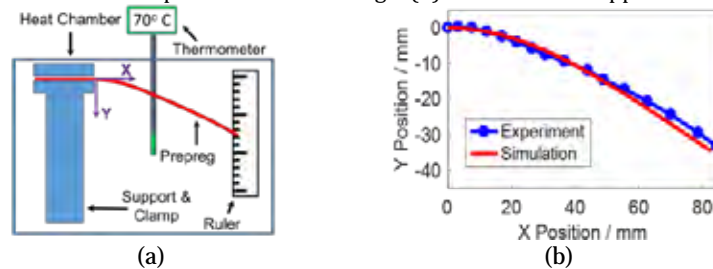


Fig. 4. (a) Experimental setup, and (b) bending shape comparison at 70°C for bending stiffness characterization.

The setup for interaction characterization is demonstrated in Fig. 5(a). It moves two prepreg layers relative to each other for the interaction characterization. A load cell records the normal and horizontal forces, whose ratio is defined as the interaction factor. One example of the histories of forces and the interaction factor in a test is shown in Fig. 5(b), while the stable value of the interaction factor

is used in FEM. The preforming process operates at the temperature ranging from 60°C to 80°C, and the characterization results at different temperatures, sliding speeds, and fiber yarn orientations are shown in Fig. 6.

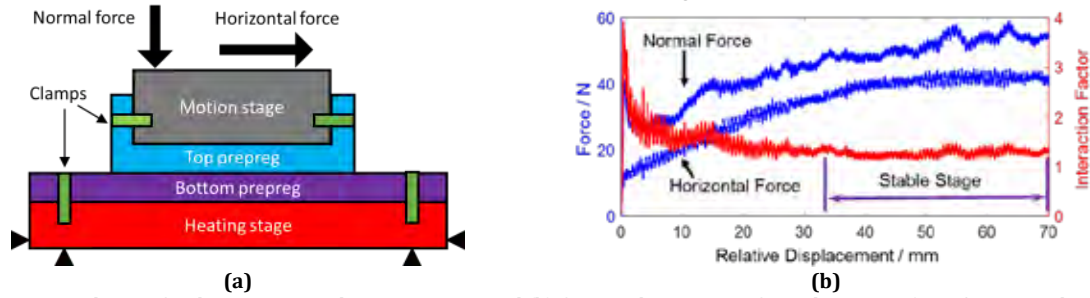


Fig. 5. (a) Experimental setup for the interaction characterization, and (b) force and interaction factor history at 5 mm/s, 70°C, 0 degree yarn angle difference

It can be seen in Fig. 6 that when the temperature is fixed, the interaction factors at various sliding speeds and fiber orientations do not change significantly. For convenience, in one preforming simulation, assuming that the temperature distribution is uniform, the interaction factor will be treated as a constant.

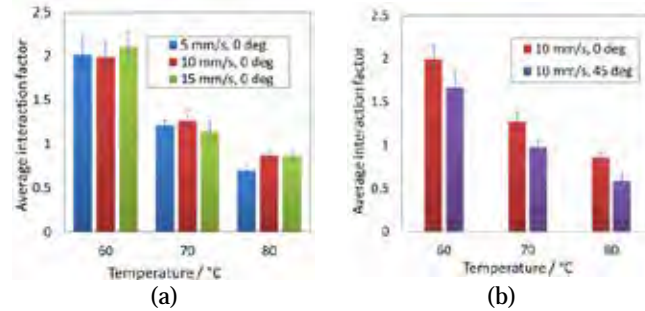


Fig. 6. Interaction factor at various temperatures subjected to different (a) relative motion speeds and (b) fiber yarn orientations.

4. Experimental validation

The double-dome test, as shown in Fig. 7, was conducted and simulated to demonstrate the capability of the material model for 3D shape forming regarding different yarn orientations and stacking sequences. The simulation model was established in LS-DYNA® using the explicit integration method. The sheet was modeled by reduced integrated shell elements. Each element is about 4 mm × 4 mm with five through-thickness integration points. The punch, binder and die were modeled by rigid shell elements.



Fig. 7. Experimental setup for the double dome test.

The simulation results in the upper-right quarter of Fig. 8 shows that the non-orthogonal material model established is capable of accurately predicting the physical experiments regarding the yarn angle distribution and blank draw-ins. For instance, the deviation of the maximum draw-in distance is about 7 mm (49 mm in experiment versus 42 mm in simulation). For comparison, an orthotropic material model (MAT_002) is utilized in another simulation whose result is shown in the upper-left quarter of Fig. 8 in the same scale as non-orthogonal model and experiment results. Since the orthotropic model cannot track the material property change during the yarns' rotation, the corresponding simulation has a maximum draw-in deviation of 24 mm, not capturing the overall process behavior.

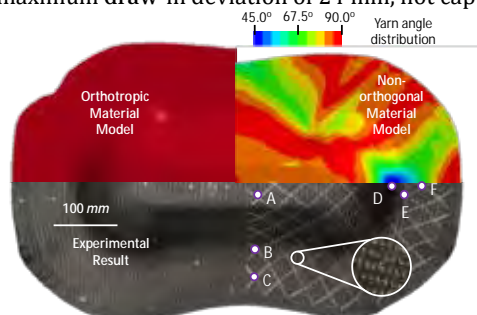


Fig. 8. Simulation and experimental results comparison of deformed geometry and yarn angle distribution for double dome preformed part of ±45° single layer woven prepreg.

In the non-orthogonal model, the yarn angle is defined as an output variable, while MAT_002 does not have the capability for direct visualization. For clarity, Table 1 compares the resulting shear angles at various locations obtained from the experiment and simulations. Again, it shows that the current model has improved the prediction accuracy.

Table 1 Resulting yarn angles from the single-layer case

Location	A	B	C	D	E	F
Experiment	80°	88°	71°	49°	56°	66°
Sim-orthotropic	70°	85°	86°	47°	59°	77°
Sim-present	81°	88°	73°	46°	60°	70°

The double-layer preforming test was conducted next. These two blanks were modeled by two layers of shell elements with different initial yarn orientations. The inter-ply interaction was simulated via the Coulomb friction model. The experimental and simulation results are shown in Fig. 9 from both top and bottom views, with both part geometry and wrinkle location marked. The simulation predicts the overall geometry and relative motion of two prepreg sheets well. The slight discrepancy might be caused by the constant interaction factor in the simulation, while in reality, it might be velocity- and pressure-dependent. Furthermore, the thickness distribution due to deformation will not be uniform, which may influence the frictional interaction and need to be captured by advanced shell elements or continuum elements.

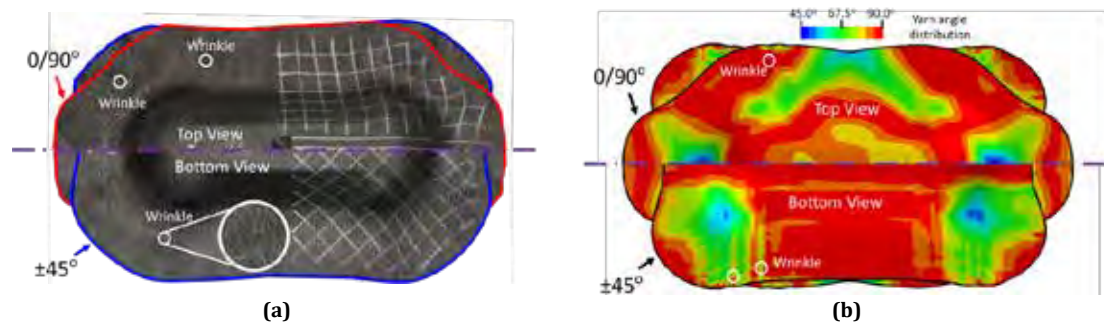


Fig. 9. Double dome preformed part of double-layer woven prepregs (a) experimental result, (b) simulation result.

5. Conclusions

An improved non-orthogonal material model that decouples the tension and shear behavior of the woven CFRPs under large shear deformation is proposed and implemented in the commercial finite element software LS-DYNA® for the composite preforming process. A systematic set of material characterization methods are developed to characterize both intra and inter-ply properties. With calibrated material properties, the material model can accurately predict the 3D deformation of the woven CFRP prepregs in preforming, demonstrated by the comparison between the simulation and experimental results from a double dome study.

Acknowledgements

This work was supported by the Office of Energy Efficiency and Renewable Energy (EERE), U.S. Department of Energy, under Award Number DE-EE0006867.

References

- [1] Teti R. Machining of Composite Materials. *CIRP Annals - Manufacturing Technology*. 2002;51(2):611-34.
- [2] Brinksmeier E, Janssen R. Drilling of Multi-Layer Composite Materials consisting of Carbon Fiber Reinforced Plastics (CFRP), Titanium and Aluminum Alloys. *CIRP Annals - Manufacturing Technology*. 2002;51(1):87-90.
- [3] Yanagimoto J, Ikeuchi K. Sheet forming process of carbon fiber reinforced plastics for lightweight parts. *CIRP Annals - Manufacturing Technology*. 2012;61(1):247-50.
- [4] Hamila N, Boisse P, Sabourin F, Brunet M. A semi-discrete shell finite element for textile composite reinforcement forming simulation. *International Journal for Numerical Methods in Engineering*. 2009;79(12):1443-66.
- [5] Cao J, Akkerman R, Boisse P, Chen J, Cheng HS, de Graaf EF, Gorczyca JL, Harrison P, Hivet G, Launay J, Lee W, Liu L, Lomov SV, Long A, de Luycker E, Morestin F, Padvoiskis J, Peng XQ, Sherwood J, Stoilova T, Tao XM, Verpoest I, Willems A, Wiggers J, Yu TX, Zhu B. Characterization of mechanical behavior of woven fabrics: Experimental methods and benchmark results. *Composites Part A: Applied Science and Manufacturing*. 2008;39(6):1037-53.

Conversion between FLD and Stress Triaxial Limit Curve

Xinhai Zhu, Li Zhang, and Yuzhong Xiao
LSTC

INTRODUCTION/MAIN FEATURES

Increasingly, as more Advanced High Strength Steels (AHSS) are being used, stamping engineers need to worry about material failure such as shear fracture during forming, in addition to the traditional necking failure. Two keywords are created in response to the users' requirement to account for the material failure modes from necking to fracture. They are:

*DEFINE_CURVE_FLD_FROM_TRIAXIAL_LIMIT, and
*DEFINE_CURVE_TRIAXIAL_LIMIT_FROM_FLD.

The FLD conversion from stress triaxial limit curve creates the corresponding necking failure limit curve when only a triaxial limit curve exists. The stress triaxial limit curve conversion from FLD curve generates the corresponding fracture limit curve when only a FLD limit curve is available.

Such conversions can be used in material models such as *MAT_037_NLP_FAILURE, *MAT_ADD_EROSION, or *MAT_260B, or in keywords such as *CONTROL_FORMING_ONESTEP.

The conversion assumes plane stress and Von-Mises yield criterion. The converted FLD or stress triaxial curve can be found in the ".o" file (a scratch file from batch queue run).

EXAMPLES:

An example of the keyword *DEFINE_CURVE_FLD_FROM_TRIAXIAL_LIMIT is listed below. Note the abscissas represent stress triaxialities, typically ranging from $-1/3$ to $2/3$; the ordinates represent equivalent plastic strains to fracture. The stress triaxial curve is referenced from the paper by Li, Yaning *et al*, "Prediction of shear-induced fracture in sheet metal forming," *Journals of Material Processing Technology*, Volume 210, issue 14, (2010).

```
*DEFINE_CURVE_FLD_FROM_TRIAXIAL_LIMIT
909
-.3284545, 2.485632
-.3193636, 2.327586
-.3102727, 2.198276
-.3011818, 2.04023
-.2875454, 1.882184
-.2739091, 1.70977
-.2602727, 1.522989
-.2466363, 1.37931
-.2239091, 1.235632
-.2011818, 1.106322
-.1648182, .9626437
-.133, .8477012
-8.754542E-02, .7471265
```

```

-4.663633E-02, .6896552
-1.481815E-02, .6465518
3.36367E-03, .632184
3.972731E-02, .6178162
8.518185E-02, .6034483
.1397273, .6034483
.1897273, .6465518
.2351819, .7183908
.2715455, .7758621
.3033637, .862069
.3306364, .9770116
.3488182, .9195403
.3715455, .8189656
.3988182, .7040231
.4351819, .5890805
.4715455, .5028736
.517, .4310345
.5533637, .4166667
.5760909, .4166667
.617, .4310345
.6397273, .4885058
.6533636, .5603449
.6670001, .8045977
*end
    
```

Figure 1 illustrates this conversion from stress triaxial curve to FLD curve. Note the red curve is the input triaxial curve and green curve is the output FLD curve from LS-DYNA. The LS-DYNA calculated FLD curve exactly matches that from the paper.

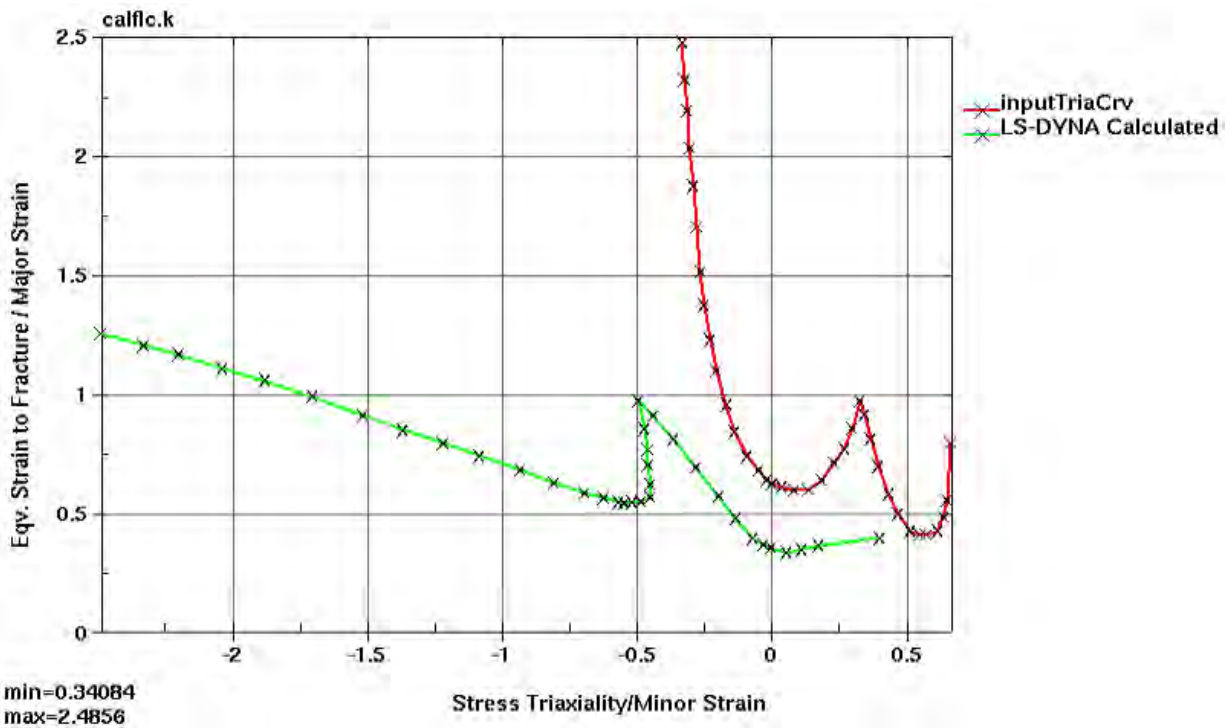


Figure 1 Conversion from Stress Triaxial Curve to FLD Curve

Another example of the keyword *DEFINE_CURVE_TRIAXIAL_LIMIT_FROM_FLD is listed below. Note the abscissas represent minor true strains of a FLD curve; the ordinates represent major true strains of a FLD curve.

```
*DEFINE_CURVE_TRIAXIAL_LIMITFROM_FLD
909
-2.485543, 1.260929
-2.326915, 1.211872
-2.196562, 1.173440
-2.037161, 1.115458
-1.876514, 1.064689
-1.701195, 0.9987057
-1.511570, 0.9169926
-1.364909, 0.8546170
-1.215432, 0.8004163
-1.080362, 0.7465187
-0.9267878, 0.6888055
-0.8039308, 0.6348159
-0.6904781, 0.5923799
-0.6199200, 0.5716710
-0.5669760, 0.5526081
-0.5458882, 0.5490728
-0.5156967, 0.5524927
-0.4797515, 0.5568793
-0.4477362, 0.5742416
-0.4447934, 0.6287722
-0.4554417, 0.7088588
-0.4556653, 0.7716601
-0.4686948, 0.8609383
-0.4924086, 0.9770012
-0.4380930, 0.9192049
-0.3606666, 0.8170972
-0.2779830, 0.6991526
-0.1942268, 0.5787448
-0.1300228, 0.4857036
-6.8558961E-02, 0.4028141
-2.8324760E-02, 0.3741716
-1.5549607E-03, 0.3616189
5.8079619E-02, 0.3408428
0.1153265, 0.3534369
0.1781329, 0.3710328
0.4022586, 0.4023391
*end
```

Figure 2 shows the conversion from the FLD curve to stress triaxial limit curve. Note the red curve is the input FLD curve and green curve is the output stress triaxial limit curve from LS-DYNA. Again, the LS-DYNA calculated stress triaxial limit curve exactly matches that from the paper.

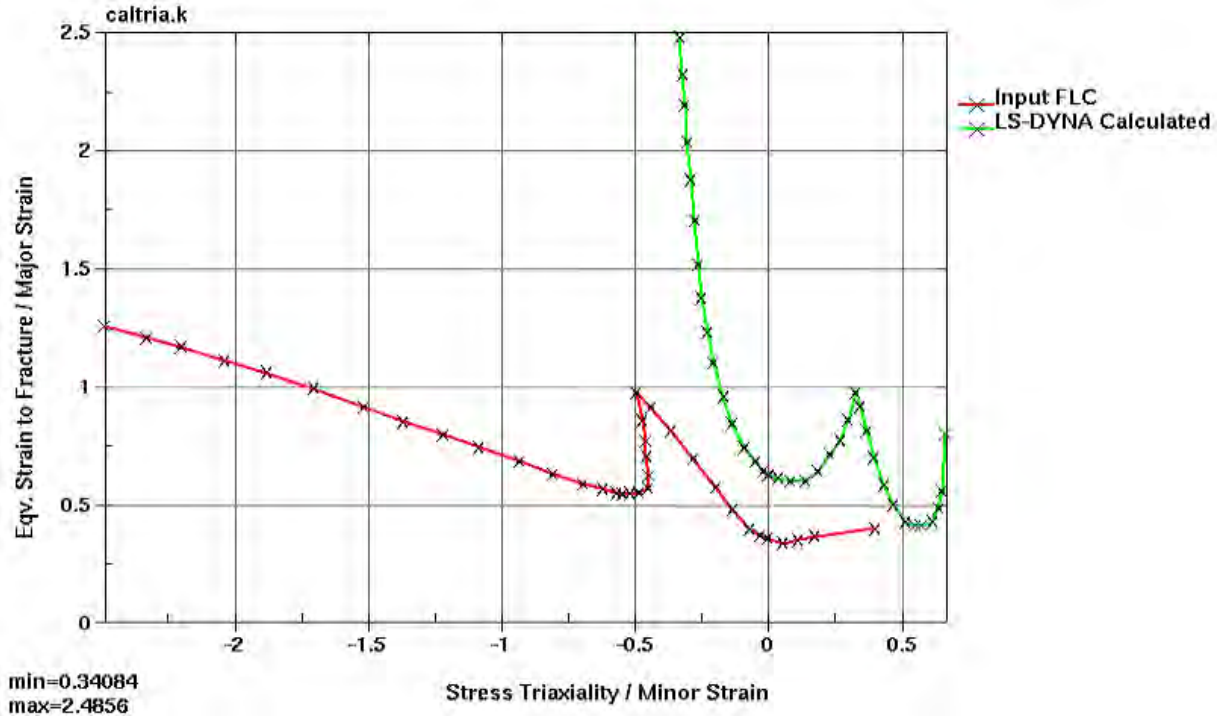


Figure 2 Conversion from FLD Curve to Stress Triaxial Limit Curve

REFERENCE:

- 1) LS-DYNA User's Manual (draft).
- 2) Li, Yaning et al, "Prediction of shear-induced fracture in sheet metal forming," *Journals of Material Processing Technology*, Volume 210, issue 14, (2010).

Best Fit GUI for Metal Forming in LS-PrePost® 4.5

Q. Yan, Xinhai Zhu, Philip Ho, Li Zhang, Yuzhong Xiao
LSTC

INTRODUCTION

Best fit technique is frequently used in sheet metal forming to assess springback accuracy. This has been done for quite a while with LS-DYNA's keyword `*CONTROL_FORMING_BESTFIT_OPTION`. The keyword requires a few entries, for example, target and source node sets, target and source mesh files, etc., which could become quite easily mixed up if done manually. In addition, one has to execute LS-DYNA to get the best fit results.

LS-PrePost Best Fit GUI:

Since the target and source node sets need to be defined in LS-PrePost, it makes sense to output the entire required keyword input from LS-PrePost, and better yet, with a single click of a button in LS-PrePost one should be able to execute the LS-DYNA run in the background and then, when the results are available, directly read into LS-PrePost for analysis, etc. It is possible to include all these functions within a GUI. A Graphical User Interface (GUI) is thus created in LS-PrePost 4.5 to do just that.

In this paper, we only showcase the features in the GUI since the best fit function in LS-DYNA has been QA'ed for quite a while and deemed very robust and reliable.

As shown in Figure 1, the GUI can be invoked by accessing the APPLICATION menu at the top left corner of the menu bar. Once the source and target parts (refer to Keyword Manual I) are imported into LS-PrePost, one can define the target part (PID 100) by selecting it from the main graphics window; similarly source part (PID 2) can be defined, shown in Figure 2. Also, there is an optional check box to output the separation distances between the two parts in vectors (`*CONTROL_FORMING_BESTFIT_VECTOR`), for optional vector display in LS-PrePost. The "Apply" button will write out the LS-DYNA output files required and start executing LS-DYNA for best fit calculation in the background. Once the best fit calculation is finished, one can get the results from LS-DYNA run by clicking on "Load Results" under the "Results" tab (Figure 4). Once the results are loaded, the "Load Results" button will turn green indicating the results are available for viewing. At this point, one can choose either display in fringe color contours the separation distances between the source and target part after the best fit (Figure 5) or display it in vectors (Figure 6). Various plot options also exist both in "Contour" or "Vector", and to turn on/off either target or source part.

There are two convenient buttons for a more detailed analysis of the best fit results. As shown in Figure 4, the "Identify" button takes you directly to *Eletol/Ident menu* so the nodes can be picked on the main screen and their separation distances displayed (Figure 7), which saves a number of

clicks. The “Section Plane” feature (Figure 4) takes you directly to *Model/Section* menu so section plane cuts can be made (Figure 8).

Note although it is transparent to the users, the necessary input files written out for LS-DYNA run are created in the running folder as shown in Figure 9, where `bestfitcontrol.k` is the main input file, which includes `bestfitcontrol_source.k` (source part mesh file in keyword format) and `bestfitcontrol_target.k` (target part mesh file in keyword format) files and `bestfit.out` is LS-DYNA result file after a best fit calculation.

Note also there is a small program (which does not require a license) called `lsdyna_bestfit.exe` must be added in the LS-PrePost4.5 installation folder, typically in `C:\Program Files\LSTC\LS-PrePost 4.5`.

REFERENCE:

LS-DYNA User’s Manual (draft).

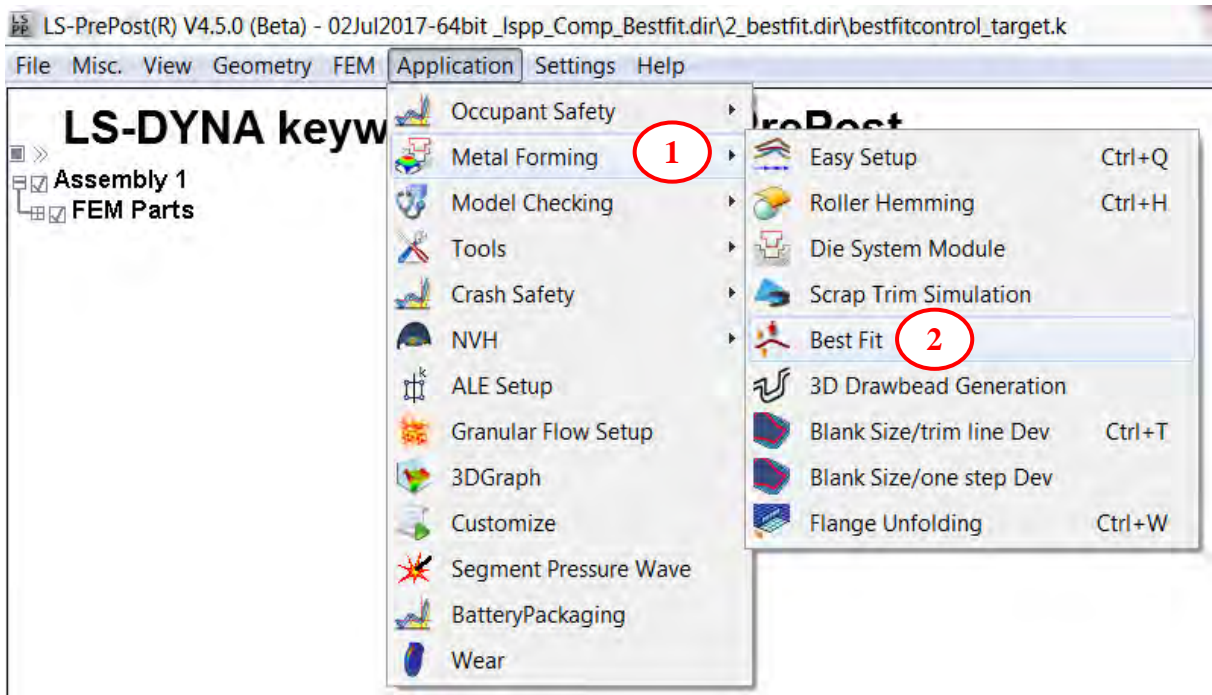


Figure 1. Activating the Best Fit GUI in LS-PrePost 4.5

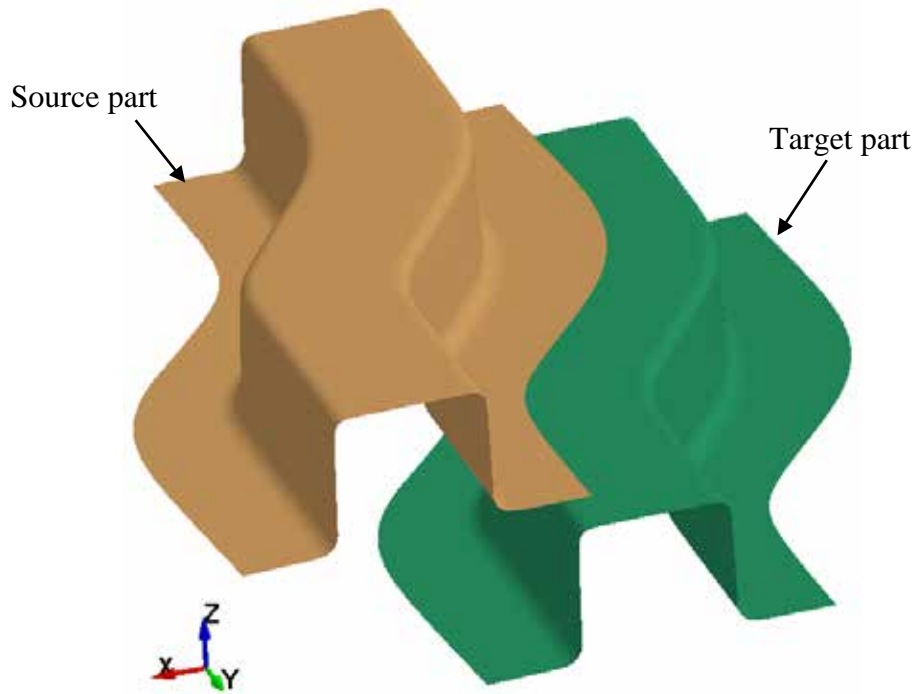


Figure 2. Target and Source Parts.

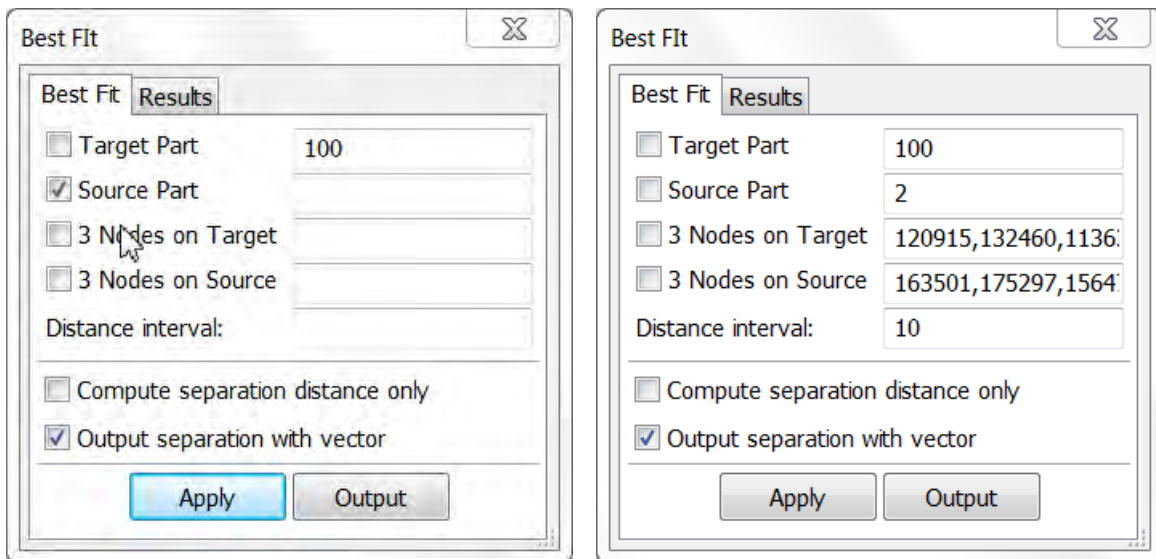


Figure 3. Define target and source parts' PIDs.

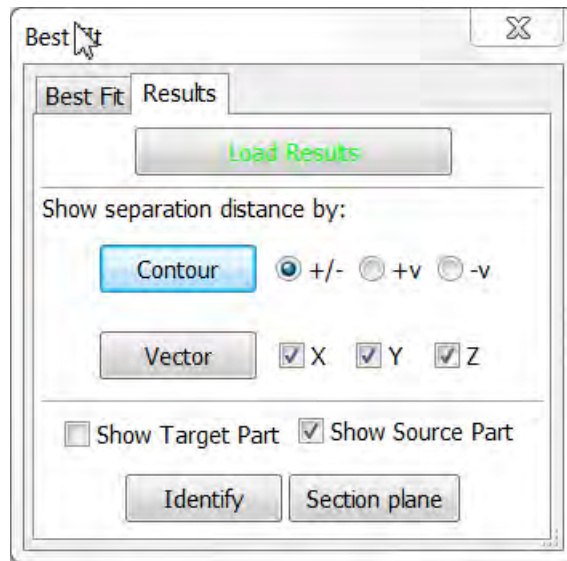


Figure 4. Loading LS-DYNA results into the GUI.

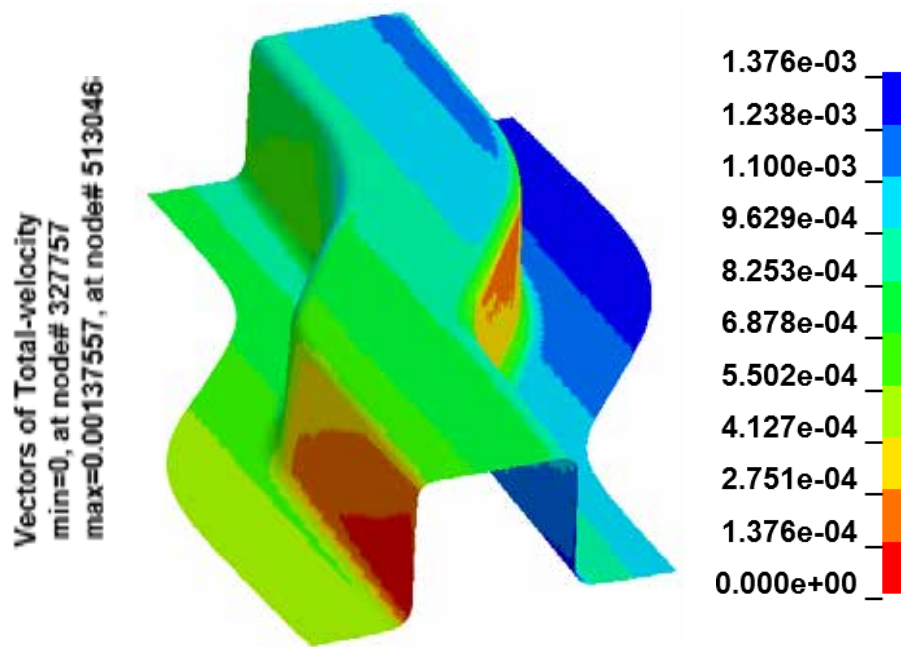


Figure 5. Color contour display of separation distances after best fitting.

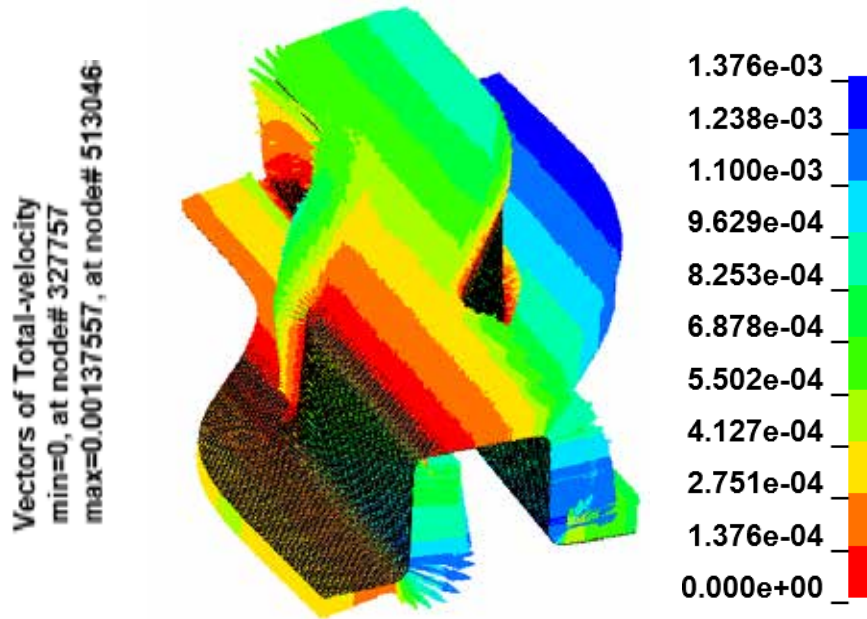


Figure 6. Vector display of separation distances after best fitting.

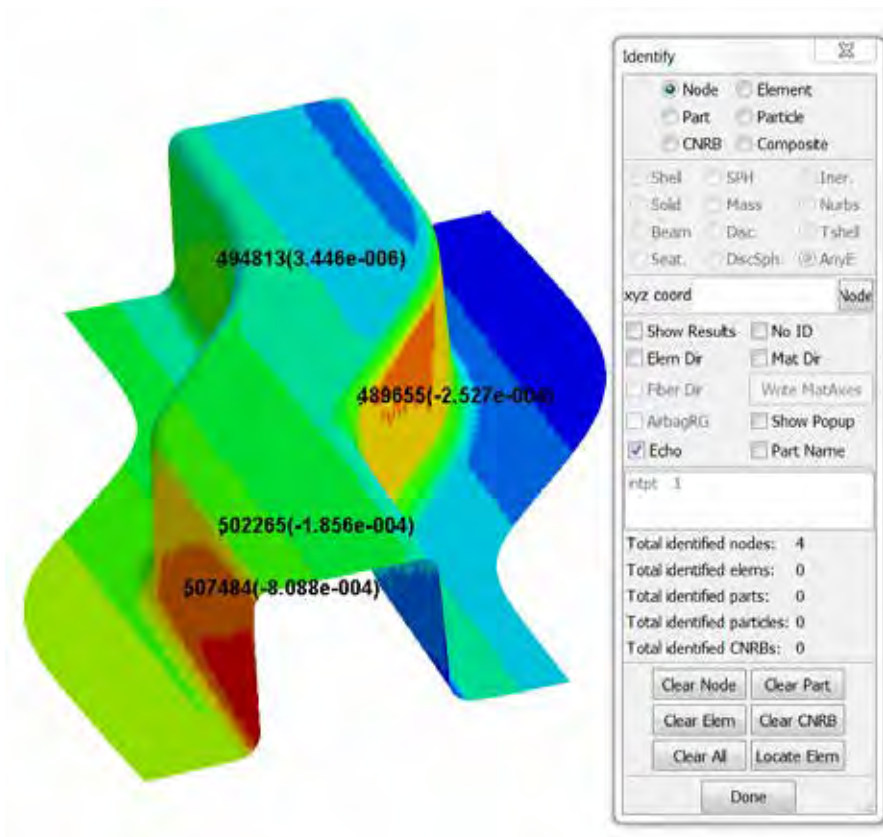


Figure 7. "Identify" separation distances between source and target parts.

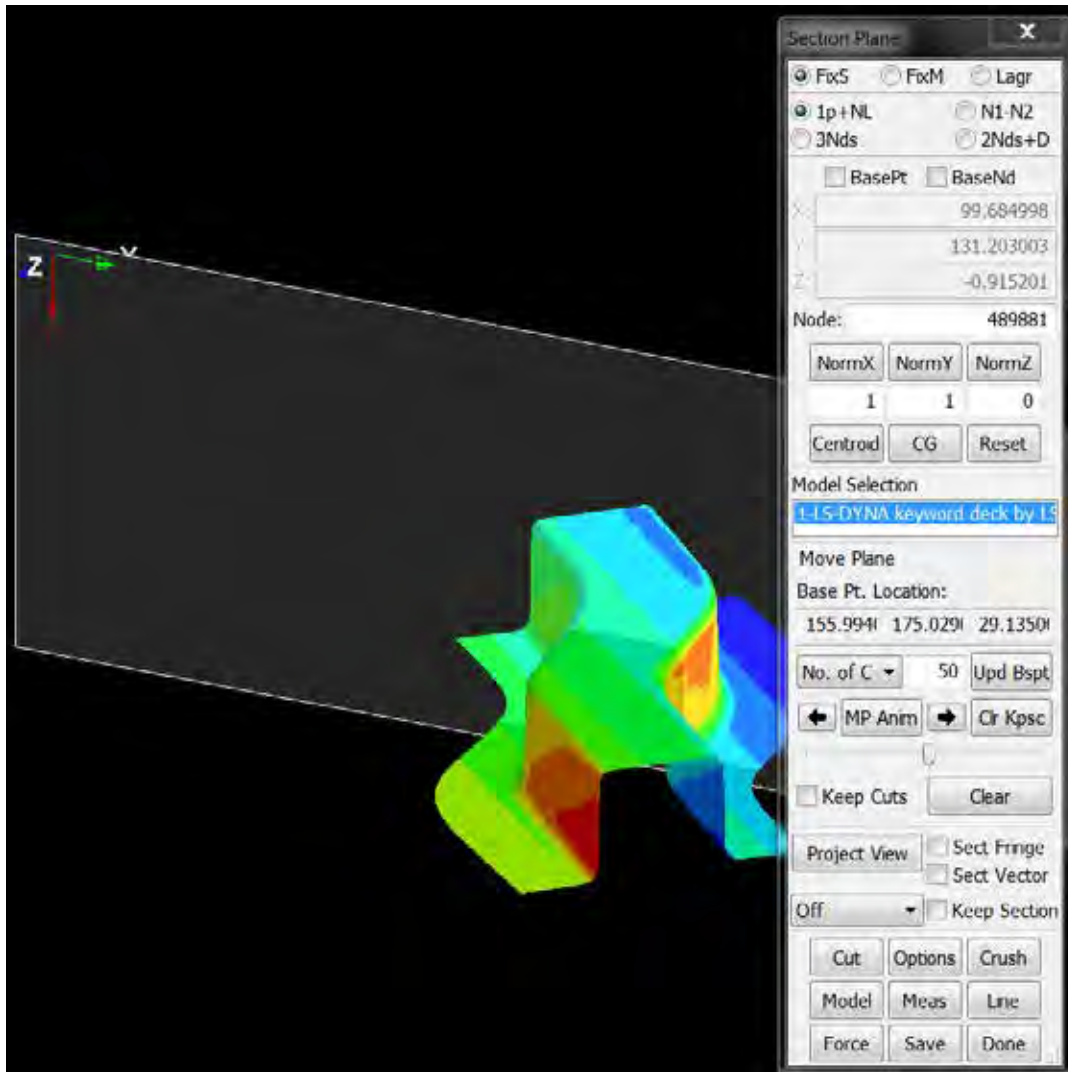


Figure 8. “Section Plane” takes you directly to the menu option for section cuts.

bestfit.out	7/7/2017 5:30 PM	OUT File	9,608 KB
bestfitcontrol.k	7/7/2017 5:29 PM	K File	1 KB
bestfitcontrol_source.k	7/7/2017 5:29 PM	K File	6,376 KB
bestfitcontrol_target.k	7/7/2017 5:29 PM	K File	6,376 KB

Figure 9. Input files generated by LS-PrePost for LS-DYNA best fit execution.